

Dynamic Response Analysis of Projectile Target Penetration Based on an FE-SPH Adaptive Coupling Method

Tianyi He ¹, Weidong Wu ¹, Yuan Zhu ¹, Yaqin Jiang ¹, Yong Mei ², Yuzheng Lv ², Jianli Shao ^{1,*} and Yunhou Sun ^{2,*}

¹ State Key Laboratory of Explosion Science and Technology, Beijing Institute of Technology, Beijing 100081, China; tianyi_900@163.com (T.H.); wd.wu93@gmail.com (W.W.); zy13753133689@163.com (Y.Z.); 13552339726@163.com (Y.J.)

² Defense Engineering Institute, AMS, PLA, Beijing 100036, China; 13730824131@139.com (Y.M.); lvyuzheng_jk@163.com (Y.L.)

* Correspondence: shao_jianli@bit.edu.cn (J.S.); houyunsun@126.com (Y.S.)

Abstract: The penetration of projectiles into targets has a broad background in engineering. In this work, numerical simulations of the projectile-target penetration problem are conducted using the Finite Element Method (FEM), the Smoothed Particle Hydrodynamics (SPH) and the Finite Element–Smoothed Particle Hydrodynamics Adaptive Coupling Method (FE-SPH ACM) based on the LS-DYNA software package. First, the penetration experiments using aluminum targets and ceramic targets are simulated. The experimental and simulation results show that the FE-SPH ACM has the better accuracy in calculating the debris cloud head velocity and interface velocity, with an error of no more than 4%. Furthermore, we use the FE-SPH ACM to investigate the anti-penetration performance of aluminum/ceramic composite targets in different combinations. We find that the reasonable layout can improve the protective performance of multi-layered target, especially composite target plates with ceramic as the front layer. In addition, the ballistic limit velocities for ceramic-aluminum ratios of 3/7, 5/5 and 7/3 are approximately 1300 m/s, 1400 m/s and 1500 m/s, respectively. Obviously, increasing the proportion of ceramic materials can enhance the anti-penetration performance.

Keywords: FE-SPH ACM; projectile-target penetration; debris cloud; composite target plate



Citation: He, T.; Wu, W.; Zhu, Y.; Jiang, Y.; Mei, Y.; Lv, Y.; Shao, J.; Sun, Y. Dynamic Response Analysis of Projectile Target Penetration Based on an FE-SPH Adaptive Coupling Method. *Metals* **2023**, *13*, 1074. <https://doi.org/10.3390/met13061074>

Academic Editors: Jean-Michel Bergheau and Håkan Hallberg

Received: 18 April 2023

Revised: 20 May 2023

Accepted: 29 May 2023

Published: 5 June 2023



Copyright: © 2023 by the authors. Licensee MDPI, Basel, Switzerland. This article is an open access article distributed under the terms and conditions of the Creative Commons Attribution (CC BY) license (<https://creativecommons.org/licenses/by/4.0/>).

1. Introduction

Penetration usually refers to the process with which a projectile penetrates or perforates an object. The research on penetration issues has involved multiple fields, such as aerospace, material science, weapon design, etc. The study of material response under penetration is of great significance. Common methods for studying penetration problems include theoretical analysis, experimental exploration, and numerical simulation methods. Because penetration problems involve large deformations, high strain rates, transient mechanics, short duration, and physical processes such as high temperature and pressure, penetration involves the destruction, deformation, and failure of projectiles and target plate materials. The fragmentation distribution law of the debris cloud after penetration and the instantaneous changes in parameters such as velocity and energy make it difficult to obtain results using theoretical and experimental methods. Numerical simulation methods are able to describe phenomena such as material damage, deformation, and fracture during penetration, and have become an important method for exploring penetration problems.

In the numerical simulation process of penetration problems, the finite element method (FEM) and smoothed particle hydrodynamics (SPH) method are commonly used methods. FEM is a numerical method based on grids, and has facilitated significant progress in many fields in recent years. Lu [1] simulated the penetration of a vibrating hammer into a large-diameter thin-walled cylinder using the FEM method, and determined the dynamic response and failure mode of the cylinder under different conditions. Liu [2]

used the FEM method to simulate the inclined penetration of reinforced concrete and obtained the penetration velocity under different inclination angles. The results are in good agreement with the experimental results. Liu [3] studied the anti-penetration performance of polyurethane/steel plate by FEM method and analyzed the residual velocity of the projectile and the energy absorption characteristics of the composite target plate. However, the FEM method also has many problems and limitations in fields such as high-velocity impact and fluid–structure interaction. When phenomena such as large deformations or crack propagation occur, the finite element method often cannot accurately reflect the problem, and the mesh elements are prone to distortion, leading to calculation termination [4,5]. When the material undergoes significant deformation, the element can fail, and after deleting the failed element, the contact interface becomes abnormal [6]. Furthermore, in numerical calculations, deleting elements can result in loss of mass, energy and momentum, and the impact results cannot be fully described. Therefore, pure finite element method is more suitable for low velocity and small deformation impact problems [7]. Improvements have been made in this area through previous research. R.M. Færgestad [8] used a coupling of FEM and DEM to study ultra-high-velocity impacts. The large deformation behavior in the local impact area was simulated using DEM, while other areas were simulated using FEM. They conducted a parametric study and investigated the sensitivity of key model parameters. In FEM, the stiffness matrix is too stiff, and the volume locking of incompressible or nearly incompressible problems leads to poor adaptability of the deformed mesh. Cui [9] proposed a smoothed finite element method based on high-order edges (ES-FEM), which provides good solutions to the aforementioned problems. In addition, to better address the shortcomings of the FEM method, meshless methods have been proposed and developed. Compared with the finite element method, the notable feature of the meshless method is that it does not require grid division. The basic idea is to remove the grid structure in the finite element method and completely replace it with a series of node arrays, which eliminates the constraints of grid initialization and grid reconstruction on the problem, ensures the accuracy of the solution, overcomes the dependence of the finite element on the grid, and shows significant advantages in problems involving mesh distortion and mesh movement [10–13]. The SPH method is a meshless method. Wang [14] proposed an analysis model to predict motion of debris clouds generated by projectiles with different shapes on multi-target plate structures and verified the accuracy of the model using SPH method, which can successfully describe the motion of debris clouds generated by hypervelocity collisions. Ju [15] studied the fragmentation characteristics of concrete based on the SPH method and proposed a predictive model. Although the SPH method does not require meshes and is good at dealing with large deformations, high pressure, high strain rates, and other issues, due to the calculation principle of the SPH method, the smooth length of particles generally has a small value, which leads to low computational efficiency. The FEM and SPH method have their own advantages and disadvantages. In order to effectively combine the advantages of the two, adaptive coupling methods of FEM and SPH (FE-SPH ACM) have been proposed [16–19] and developed. He [20] reproduced the process of metal projectile penetrating metal target plate by FE-SPH ACM and proposed a statistical analysis method for fragments. Based on the FE-SPH ACM, Chen [21] established a general analysis method for dangerous fragments in debris cloud. Wen [22] analyzed fragmentation patterns under different impact conditions through the FE-SPH ACM based on the propagation and evolution of shock waves. Scazzosi [23] simulated hypervelocity impacts of bullets on ceramics using the FE-SPH ACM and compared it with commonly used methods in the finite element method. Kala [24] simulated penetration problems of concrete-like materials by FE-SPH ACM and demonstrated that more accurate results can be obtained compared with the FEM method in terms of penetration depth and failure area. Cottrell [25] compared three techniques for simulating hypervelocity impact on ceramics: numerical material erosion, mass-conserving adaptive re-meshing, and finite element conversion to meshless particles.

However, current research lacks a systematic understanding of the ability of using different methods to simulate hypervelocity penetration and target plate fragmentation issues. In this paper, numerical simulations of the projectile-target penetration problem are conducted using Finite Element Method (FEM), Smoothed Particle Hydrodynamics (SPH) and Finite Element–Smoothed Particle Hydrodynamics Adaptive Coupling Method (FE-SPH ACM) using the LS-DYNA software package. The applicability of the three methods is compared by combining the experimental and simulation results, and the process of fragment evolution is analyzed.

2. Numerical Methods

2.1. FE-SPH ACM Principle

The principle of the FE-SPH ACM [26] is to use the FEM for calculation at the initial moment, automatically converting elements in the large deformation area into particles during the calculation process, and using the SPH method for calculation. When the distortion element reaches the criterion set value, it will automatically be converted to an SPH particle. At the same time, the method also incorporates the SPH algorithm, the finite element–particle coupling algorithm and the finite element–particle contact algorithm. The variables of the converted element, such as stress, strain, Internal energy, and damage are transferred to the particle points. The mass, velocity, and center of mass of the particles are the same as those of the original elements, and the particle velocity is calculated from the momentum of the original element.

2.2. Exact Solution of Debris Cloud

In response to the debris cloud formed by target penetration, Bless [27] proposed a debris cloud model through theoretical derivation, and obtained three axial characteristic parameters describing the motion of the debris cloud using one-dimensional shock wave theory. These parameters are the head velocity v_1 , interface velocity v_2 , and tail velocity v_3 . According to the shock wave theory in the solid of the hypervelocity impact field, qualitative analysis results show that a strong shock wave will form after the projectile collides with the target. Based on the one-dimensional shock wave theory, the velocity difference of particles before and after the shock wavefront can be obtained, as shown in Formula (1).

$$u = v_0 \left(1 + \left[\frac{\rho_{0b}(1 - \rho_{0p}/\rho_{1p})}{\rho_{0p}(1 - \rho_{0b}/\rho_{1b})} \right]^{1/2} \right)^{-1} \quad (1)$$

where v_0 is the initial impact velocity, ρ_{0b} and ρ_{1b} are the densities of the target before and after the impact, respectively. In addition, ρ_{0p} and ρ_{1p} are the densities of the projectile before and after the impact, respectively. The particle velocity in the target is u , and that in the projectile is $(v_0 - u)$ after the shock wave impact. Under the influence of sparse waves, the pressure in the material is unloaded to zero and the material further accelerates. Using one-dimensional shock wave theory, the expressions for v_1 , v_2 , and v_3 can be obtained as follows:

$$v_1 = 2u \quad (2)$$

$$v_2 = 2u - v_0 \quad (3)$$

$$v_3 = u \quad (4)$$

The above is the Bless model based on one-dimensional shock wave theory to describe the motion of the debris cloud. The velocity calculated by this model matches well with that of a spherical projectile and has moderate agreement with that of a cylindrical projectile. Therefore, the Bless model can be combined with experimental results as an accurate solution for the expansion velocity of the debris cloud to verify the accuracy of the debris cloud velocity calculated using different numerical simulation methods.

3. Numerical Simulation of Aluminum Projectile-Target Penetration Experiment

As a ductile material, the use of metals has resulted in systematic progress in the research of different projectiles [28,29], cross-sectional shapes [30,31], and impact angles [32,33] during penetration. Therefore, numerical simulation methods have been widely used in ductile target plates. In this section, with reference to Piekutowski's experiment [34], which involved the hypervelocity impact of a spherical projectile on a target plate, two polar aurora air guns were used to launch aluminum bullets impacting an aluminum alloy target plate. By controlling the impact velocity of the aluminum bullets and changing the ratio of the projectile diameter to the target plate thickness, the factors affecting the characteristics of the debris cloud were explored.

3.1. Computational Model

In this paper, LS-DYNA finite element software was used to simulate and establish FEM, SPH, and FE-SPH calculation models for the impact of aluminum alloy projectiles on aluminum alloy target plates. The specific geometric parameters are shown in Figure 1. In the figure, the projectile (in red) and the target plate (in blue) are hexahedral Lagrangian elements. The projectile has a diameter of 9.53 mm and is made of 2017-T4 aluminum alloy, with a velocity of $v = 6680$ m/s. The target plate is a square plate with a width of 50 mm and a thickness of 0.8 mm, made of 6061-T6 aluminum alloy. In the FE-SPH ACM calculation, the keyword `DEFINE_ADAPTIVE_SOLID_TO_SPH` is used to convert both the projectile and the target plate from FEM elements to SPH particles, and the failure criterion is set. In this paper, the failure criterion is set as the maximum principal strain failure, and the FEM elements are converted to SPH particles after the principal strain reached 1.2.

The Johnson–Cook (JC) strength model and Mie–Grüneisen equation of state were selected to characterize the materials. The Johnson–Cook constitutive equation [35] describes the strengthening of material yield stress under the combined action of material softening and strength reduction caused by strain, strain rate, and temperature rise. The Mie–Grüneisen equation of state is mainly used to describe the thermodynamic behavior of most metals in the solid state. These two models are the most commonly used models in numerical simulations, and are suitable for high-strain-rate situations such as hypervelocity impact. The maximum tensile stress failure criterion and the JC failure model are used to simulate tensile failure and compressive failure, respectively. In previous studies, aluminum alloy has been a relatively common and widely used material, so the material model parameters can be taken from [20]. The specific parameters are shown in Table 1.

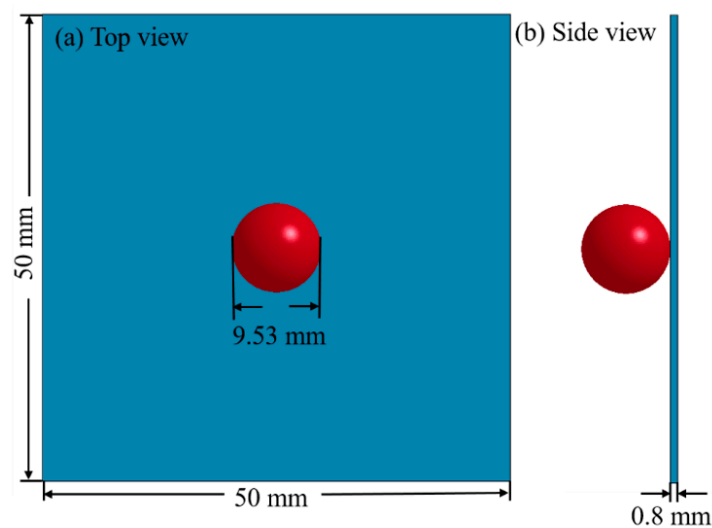


Figure 1. Numerical calculation model of 2017-T4 aluminum alloy projectile penetration into 6061-T6 aluminum alloy target plate. (a) Top view; (b) side view.

Table 1. Material model parameters.

Parameter	2017-T4	6061-T6
Johnson–cook		
RO (kg/m ³)	2770	2770
G (Pa)	2.76×10^6	2.76×10^{10}
PR	0.33	0.33
A (Pa)	2.65×10^8	2.90×10^8
B (Pa)	4.26×10^8	2.03×10^8
N	0.34	0.35
C	0.015	0.011
M	1.089	1.089
SPALL	3	3
D1	0.8	1.0
D2	0	0
Mie–Gruneisen		
C	5368	5368
S1	1.339	1.339
GAMAO	1.97	1.97

3.2. Comparison of Results Using Different Simulation Methods

Figure 2 shows the evolution process at different times obtained by simulation and calculation using three different methods under an impact velocity of 6680 m/s. From the figure, it can be seen that both the projectile and target plate were shattered after being subjected to the impact of the projectile. Initially, the edge of the impact area was damaged, and then the convexity of the target plate gradually increased, causing element failure and significant deformation of the projectile. Obviously, the simulation results under the FEM method showed that both the target plate and the projectile had deleted elements, which could observe the movement information of large debris but could not simulate the effect of particle splashing. The SPH method was able to obtain a perfect debris cloud, but could not obtain the situation of large debris. The simulation results of FE-SPH ACM combine the characteristics of the above two methods, making it possible to observe the situation of the debris cloud and directly obtain information on large debris that is more accurate than SPH. Based on the obtained parameter information, such as the shape, size, energy, and distribution of debris, statistical analysis can be performed later. In addition, under the FE-SPH ACM, FEM elements need to fail and be converted into SPH particles to form the debris cloud, so it can be clearly seen from the figure that the size of the debris cloud simulated by FE-SPH ACM is smaller than that with SPH, especially for the ricochet debris cloud located in the front end of the target and the debris cloud at the tail of the projectile.

Figure 3 presents the motion curves of the projectile calculated by different simulation methods at an impact velocity of 6680 m/s. From Figure 3a, it can be seen that the velocity curve drops sharply at first, because the projectile has penetrated the target plate, and then the curve becomes stable. At the same time, the remaining velocity of the projectile is highest under the FEM method (approximately 6340 m/s), while it is lowest under the SPH method (approximately 6100 m/s), and the remaining velocity calculated by FE-SPH ACM is about 6250 m/s. This is because under the FEM method, elements of the target plate are deleted after the damage threshold is reached, and the subsequent calculation reduced the loss of the projectile's velocity. However, some elements of the projectile also reach the failure criterion, so under the FE-SPH ACM, some elements of the projectile are converted into SPH particles, leading to a higher remaining velocity of the projectile than under the SPH method. Figure 3b shows the energy curve of the projectile over time. Under the FEM method, the energy curve of the projectile always decreases. Under the SPH method, the energy curve of the projectile stabilizes after a period of decline. Under the FE-SPH ACM, the energy curve of the unconverted FEM elements always shows a decreasing trend until they have all been converted into SPH particles. The energy curve of the converted SPH

particles always shows an increasing trend until it has stabilized. Adding the energy curve of the two together, it can be found that the energy curve of the FE-SPH ACM shows the same trend as that of the SPH method, verifying the rationality of this method.

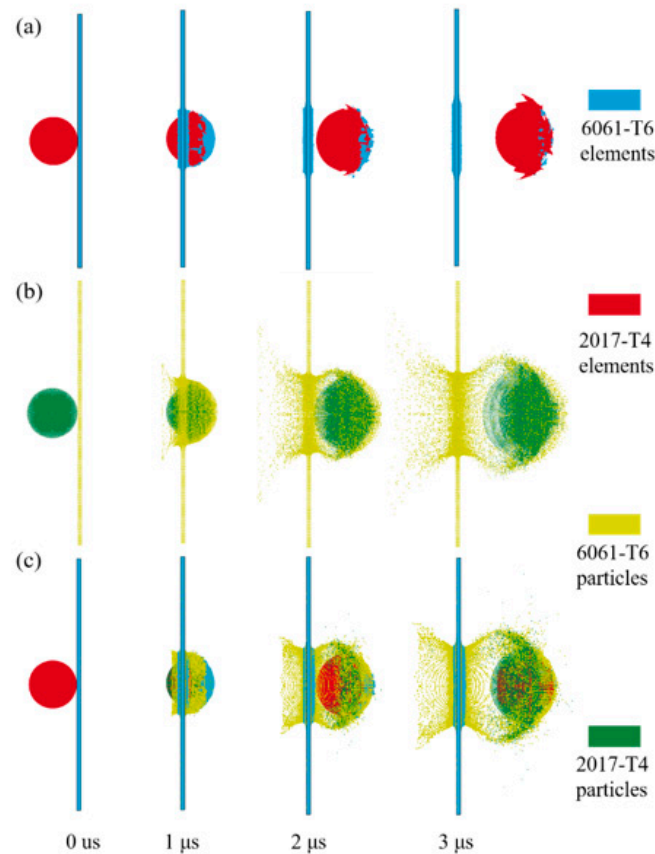


Figure 2. Evolution images obtained at different times using different numerical simulation methods at an impact velocity of 6680 m/s. (a) FEM; (b) SPH; (c) FE-SPH ACM.

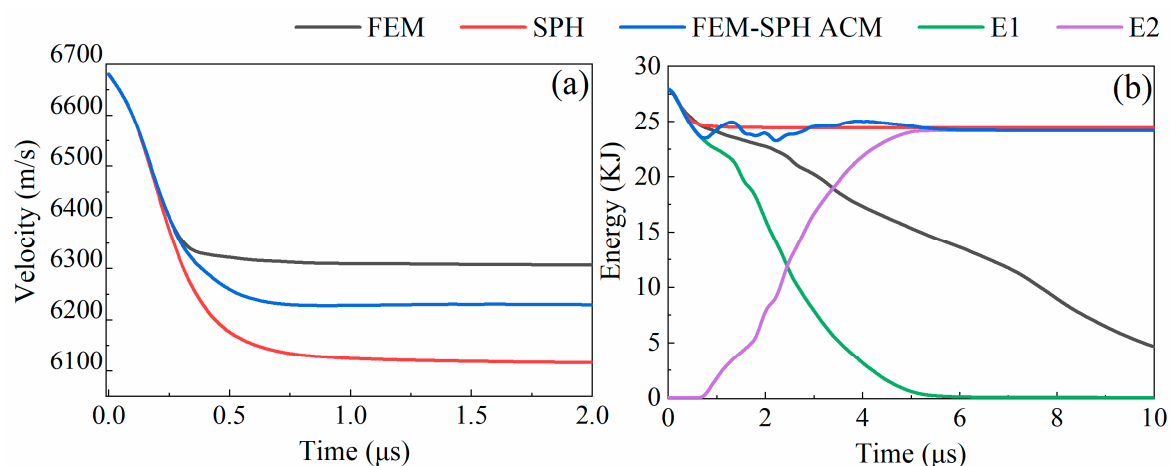


Figure 3. The motion curves of the projectile calculated using different simulation methods at an impact velocity of 6680 m/s. (a) The curve of velocity change with time. (b) The curve of energy change with time, where E1 is the unconverted FEM elements energy under the FE-SPH ACM, and E2 is the converted SPH particles energy under the FE-SPH ACM.

To further validate the accuracy of the simulation results, the numerical simulation results at 10 μ s were obtained with reference to the experimental results of Piekutowski [34], as shown in Figure 4. It can be seen from Figure 4a–c that the FEM method can only obtain

the final shape of the projectile and target plate, and cannot obtain information about the debris cloud and particles. Both the SPH method and the FE-SPH ACM can obtain the shape of the debris cloud. The distance from the farthest fragment to the target plate is defined as the maximum distance of the debris cloud, denoted as h . The characteristic parameters of the front end of the debris cloud, denoted as a_1 , a_2 , and a_3 , were defined, and the errors of the three methods and the experimental method were compared. Meanwhile, according to the debris cloud model derived from theoretical derivation by Bless [27], three characteristic velocities v_1 , v_2 , v_3 of the debris cloud are calculated, and the errors between the computational results of the three methods and the exact solution are compared. As shown in Table 2. It can be seen from the table that the maximum distances calculated by the three methods are similar (45.447 mm for FEM, 44.497 mm for SPH, 44.682 mm for FE-SPH ACM), and the errors are relatively small and within an acceptable range. However, in terms of the characteristic parameters of the debris cloud, the error of the FE-SPH ACM is smaller than that of the SPH. In terms of the characteristic velocities of the debris cloud, the FE-SPH ACM method calculates a larger result than the SPH method, with smaller v_2 error in FE-SPH ACM calculation and smaller v_3 error in SPH calculation. Overall, it can be concluded that the FE-SPH ACM method is both accurate and effective.

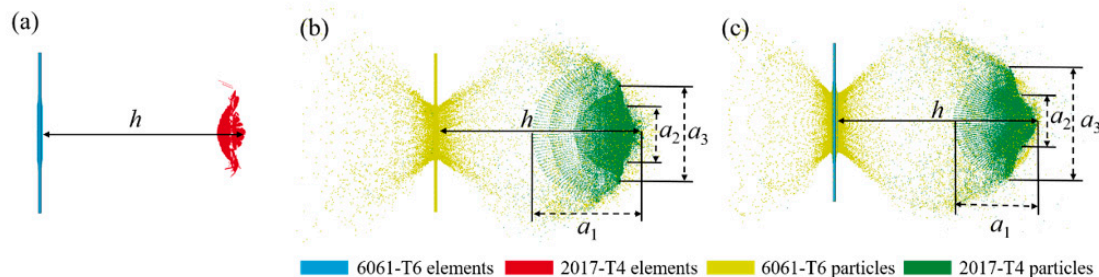


Figure 4. The results of different numerical simulation methods at 10 μ s and the definition of characteristic parameters. (a) FEM, (b) SPH, (c) FE-SPH ACM. h represents the maximum distance of the debris cloud, and a_1 , a_2 , and a_3 represent the characteristic parameters of the debris cloud.

Table 2. The error between the characteristic parameters obtained by different numerical simulation methods and the experiment, and the error between the characteristic velocity and the exact solution.

Parameter	Experiment [34]	Exact Solution [27]	FEM	Error	SPH	Error	FE-SPH ACM	Error
h (mm)	41.932	/	45.447	7.73%	44.497	6.12%	44.682	6.56%
a_1 (mm)	19.060	/	/	/	21.022	10.29%	20.045	5.17%
a_2 (mm)	14.295	/	/	/	16.067	12.40%	15.178	6.18%
a_3 (mm)	23.825	/	/	/	25.474	6.29%	24.712	3.72%
v_1 (m/s)	/	5929.52	6290	6.08%	6120	2.71%	6120	2.71%
v_2 (m/s)	/	5936.16	/	/	5590	5.83%	5740	3.30%
v_3 (m/s)	/	3359.04	/	/	3630	8.07%	3740	11.34%

Based on the numerical simulation results of the FE-SPH ACM, information such as the distribution of fragments during the impact process can be obtained. Figure 5 shows the evolution process of large fragments calculated by the FE-SPH ACM. It can be seen from Figure 5 that large fragments mainly exist in the form of FEM elements, and when the maximum principal strain of the elements reaches the failure criterion of 1.2, the FEM elements in the large fragments are converted into SPH particles, resulting in a reduction in the size of the large fragments. Figure 6 shows the fragment distribution maps at different times and the curve of the number of large fragments over time under the FE-SPH ACM. It can be seen from Figure 6 that large fragments mainly distribute in the central area of the bullet hole, i.e., the head of the projectile. In the initial stage of fragment formation, the fragments gather together, and the number of elements is relatively large. Then, some

of the elements fail and are converted into SPH particles, and the fragments begin to break into smaller pieces. With increasing time, the number of debris elements tends to exponentially decrease.

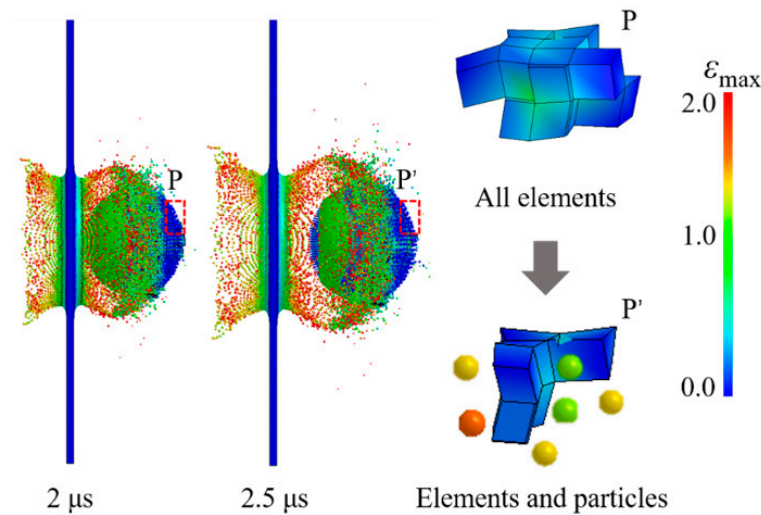


Figure 5. Schematic diagram of the process of converting FEM elements into SPH particles when the maximum principal strain reaches 1.2 under the FE-SPH ACM.

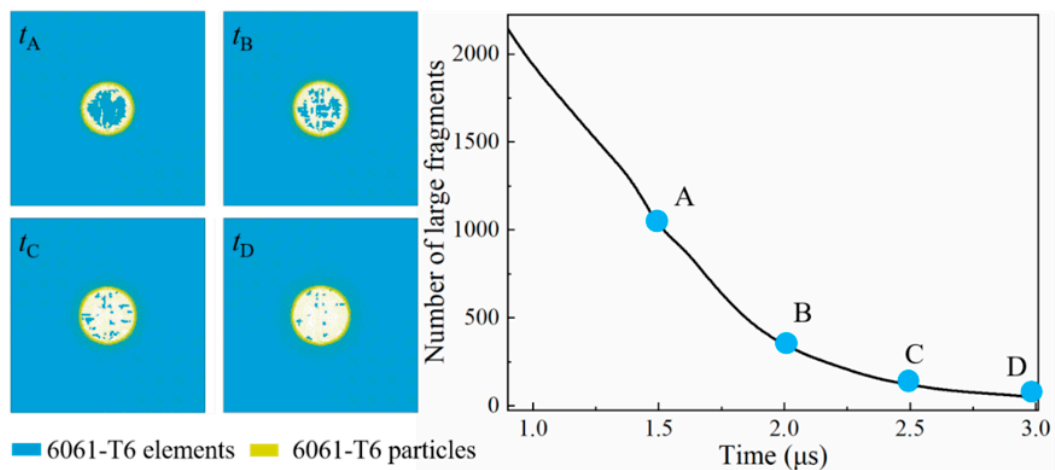


Figure 6. Fragment distribution maps at different times and the curve of the number of large fragments over time under the FE-SPH ACM.

In summary, the accuracy and superiority of FE-SPH ACM in simulating the penetration of aluminum alloy projectiles into aluminum alloy target are verified by comparing the numerical simulation results of three methods. Obviously, FE-SPH ACM can simulate the debris cloud and large debris information during the penetration process, making it applicable to high-velocity penetration problems involving aluminum alloy target plates.

4. Numerical Simulation of Tungsten–Ceramic Projectile–Target Penetration Experiment

Brittle materials are also commonly used as target plates in penetration problems. Ceramic materials, as a type of brittle material, have excellent mechanical properties and are widely used in protective applications [36]. In this section, we refer to the experimental work of S. Nemat-Nasser [37], who considered a tungsten alloy flat-headed projectile impacting a pure ceramic target plate at a velocity of 903.9 m/s.

4.1. Computational Model

The model is established using LS-DYNA software, where the projectile is modeled as a cylindrical object with a diameter of 6.14 mm and a length of 20.86 mm, and the material is tungsten alloy. The target plate is modeled as a square with dimensions of 101.6 mm × 101.6 mm and a thickness of 12.7 mm, and the material is aluminum oxide ceramic. All elements are hexahedral Lagrangian elements. When using the FE-SPH ACM for calculations, the target plate is set as a keyword (DEFINE_ADAPTIVE_SOLID_TO_SPH) to convert the FEM element into SPH element.

The Johnson–Cook (JC) strength model and Mie–Gruneisen equation of state are chosen to characterize the tungsten alloy material, with parameters taken from references [38,39], as shown in Table 3. The MAT_JOHNSON_HOLMQUIST_CERAMICS model (referred to as the JH2 model), which is commonly used to simulate the mechanical behavior of brittle materials such as ceramics under impact and penetration [40,41], is chosen to characterize the ceramic material. Material model parameters are taken from reference [23] and are shown in Table 3.

Table 3. Material model parameters.

JC Model Parameters		JH2 Model Parameters	
Parameters	Tungsten Alloy	Parameters	Ceramic
RO (kg/m ³)	17,160	RO (kg/m ³)	3920
E (Pa)	4.10×10^{11}	G (Pa)	1.524×10^{11}
PR	0.28	A	0.93
A (Pa)	1.20×10^9	B	0.31
B (Pa)	1.41×10^8	C	0
N	0.12	M	0.6
C	0.016	N	0.6
M	1.00	EPSI	1
SPALL	3	T (Pa)	2.0×10^8
D1	0	SFMAX	0.2
D2	0.33	HEL (Pa)	1.9×10^{10}
D3	−1.5	PHEL (Pa)	1.46×10^9
D4	0	BETA	1
C	4029	D1	0.005
S1	1.23	D2	1
GAMAO	1.54	K1 (Pa)	2.54×10^{11}
		K2	0
		K3	0
		FS	7.0×10^{-4}

4.2. Comparison of Results Using Different Simulation Methods

Figure 7 shows the evolution images at different times obtained through different numerical simulation methods at an impact velocity of 903.9 m/s. From the figure, it can be seen that when using the FEM method for calculation, due to the removal of failed ceramic target plate elements, the tungsten alloy projectile only undergoes a small deformation at its head, without significant damage, making it impossible to simulate the effect of particle splashing. When using the SPH method for calculation, since the elements exist in the form of particles, they will not be removed after failure, resulting in the formation of a debris cloud and more obvious deformation of the projectile. However, when using the FE-SPH ACM for calculation, as the elements that fail will transform into SPH particles and continue to participate in the calculation, the projectile will undergo significant deformation, and a debris cloud will be formed. From the figure, it can be seen that both the SPH method and the FE-SPH ACM can obtain the shape of the debris cloud, and the latter can also obtain information about large fragments contained in the debris cloud. In addition, under FE-SPH ACM, the FEM elements need to fail and transform into SPH particles to form the debris cloud, so the size of the debris cloud simulated by the FE-SPH ACM is smaller than

that of the SPH method, especially for the ricochet debris cloud located at the front end of the target.

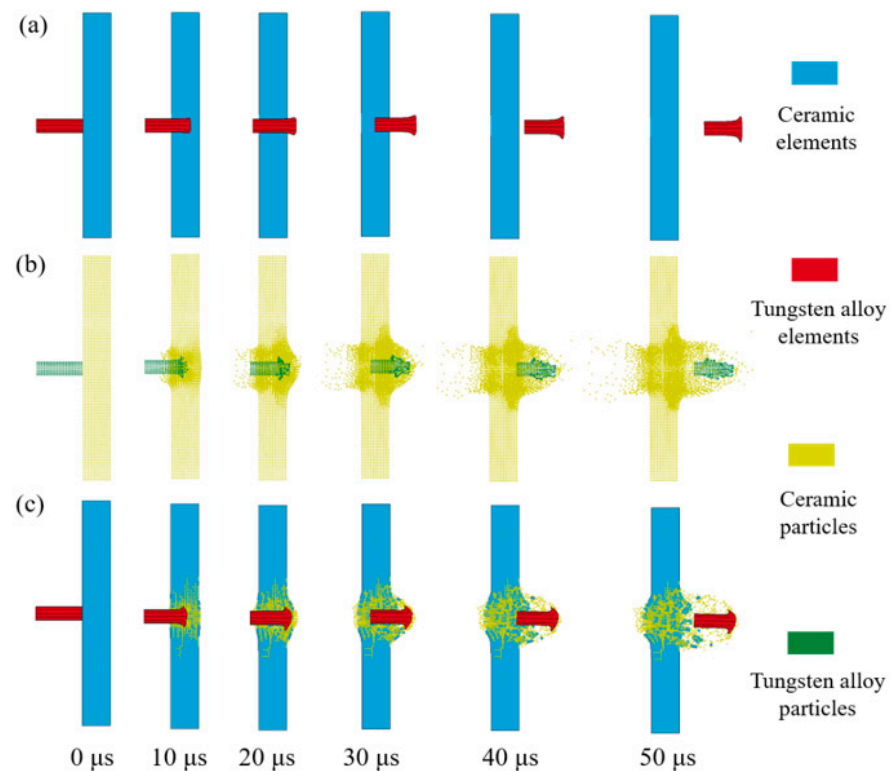


Figure 7. Evolution images at different times obtained through different numerical simulation methods at an impact velocity of 903.9 m/s. (a) FEM; (b) SPH; (c) FE-SPH ACM.

Figure 8 shows the shape of the projectile and the main strain cloud map at different times obtained by simulating through three methods. It can be seen from the figure that the deformation of the projectile mainly occurs in the head, and the degree of deformation of the projectile simulated by the three methods will be different. Under the FEM method, the projectile undergoes an upset, the range of deformation is the greatest, and the reduction in projectile length is the greatest. Under the SPH method, particles form into splinters. Under the FE-SPH ACM method, the projectile peels off in a petal shape and presents a mushroom-head shape, with a small range of deformation and the least reduction in projectile length.

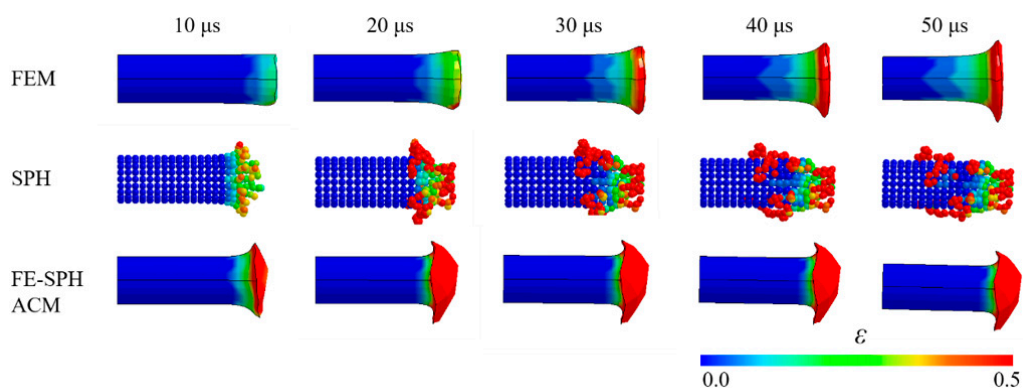


Figure 8. Principal strain cloud maps calculated by different simulation methods at different times.

Figure 9 presents the motion curves of the projectile calculated using different simulation methods at an impact velocity of 903.9 m/s. Figure 9a is the curve of the velocity

change with time, and Figure 9b is the curve of the energy change with time. As can be seen from the figure, the velocity curve of the projectile first decreases, and then the projectile penetrates the target plate, and the velocity curve becomes stable. In the FEM method, some elements will be removed due to failure during the penetration process, so there is not much change in the projectile's velocity. However, in the SPH method, failed elements will not be removed during calculation, and the failed elements in the FE-SPH ACM are transformed into SPH particles. Therefore, the velocity curve under these two methods will experience a significant decline, and the velocity curve under the SPH method will decrease faster. At the same time, due to the high failure criterion of the tungsten alloy projectile, there are not many failed elements in the projectile, so there is little difference in the final velocity under these two methods. The energy curve of the projectile shows a similar trend to the velocity curve.

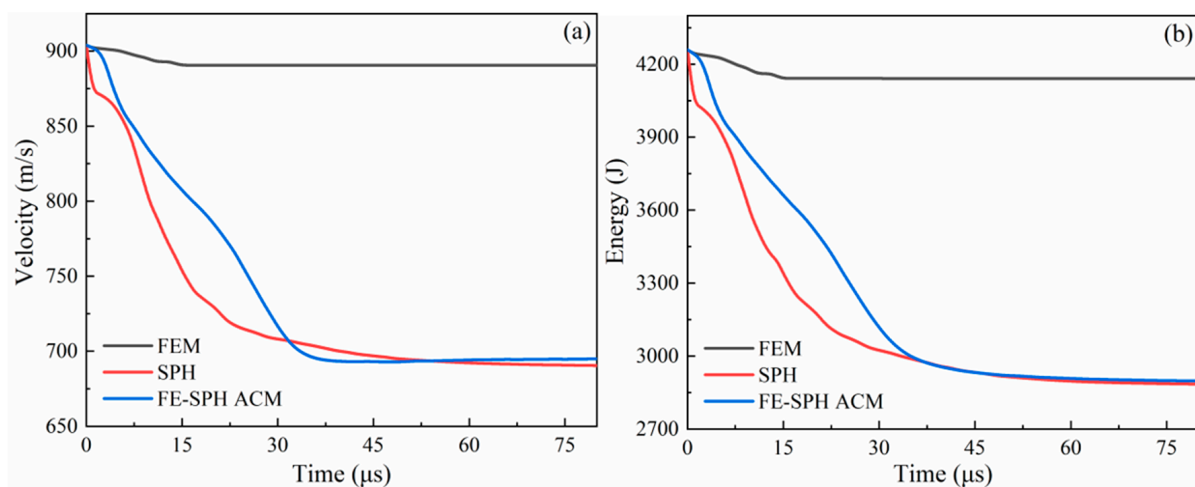


Figure 9. The motion curves of the projectile calculated by different simulation methods at an impact velocity of 903.9 m/s. (a) The curve of velocity change with time. (b) The curve of energy change with time.

Furthermore, we compared the residual velocities calculated using three simulation methods with the experimental results [37], as shown in Table 4. From Table 4, it can be seen that the simulation results using the SPH method and FE-SPH ACM are in good agreement with the experimental results (1.03% error for SPH and 1.76% error for FE-SPH), while the calculation results using the FEM method differ significantly from the experimental results (30.5% error for FEM). This verifies the accuracy of the SPH method and FE-SPH ACM.

Table 4. Calculation results and errors of residual velocity.

	Experiment	FEM	SPH	FE-SPH
Residual velocity (m/s)	682	890	689	694
Error	/	30.50%	1.03%	1.76%

Additionally, based on the numerical simulation results of the FE-SPH ACM, information about the fragments during the penetration process can be obtained. However, since ceramic materials belong to the brittle materials, the number of pieces of large debris is not easy to count, unlike in the case of ductile materials. Therefore, the number of failed FEM elements was counted here. Figure 10 shows the penetration process of the projectile at different times and the curve of the number of failed elements changing with time. As can be seen from Figure 10, during the penetration process of the projectile, the failed elements are mainly concentrated in the head of the projectile, and some of them form large fragments, which eventually transform into SPH particles, forming a debris cloud. From the curve, it can be seen that the failed elements mainly form at the beginning of the

penetration process, and the number of failed elements becomes stable after the projectile passes through the target board.

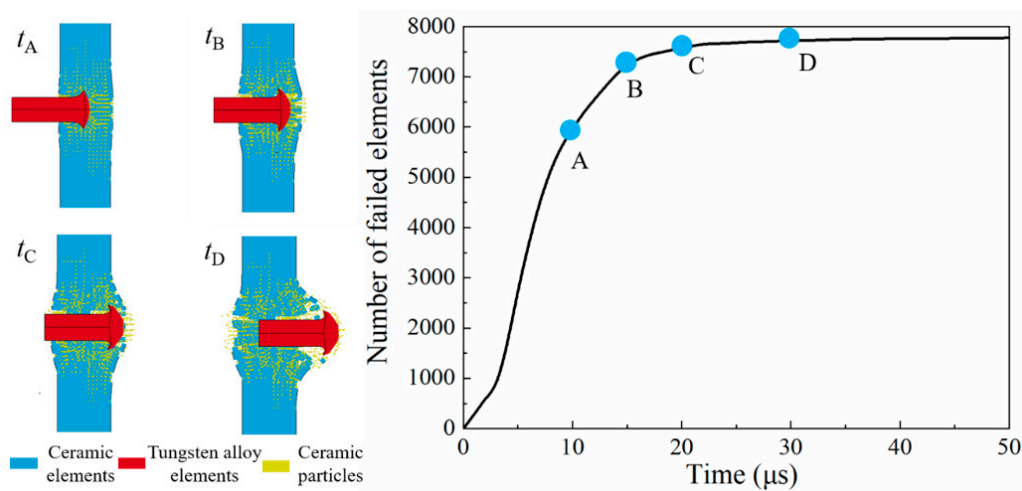


Figure 10. Fragment evolution images at different times and time-dependent curves of the number of failed elements.

In summary, the accuracy and superiority of FE-SPH ACM in simulating the penetration of tungsten alloy projectiles into ceramic target are verified by comparing the numerical simulation results of three methods. This method not only ensures high accuracy and efficiency, but also provides information about the evolution of fragments. Therefore, the FE-SPH ACM can be applied to the numerical simulation of high-velocity penetration of ceramic targets.

5. Numerical Simulation of the Projectile Composite Target Penetration Experiment Based on the FE-SPH ACM

As mentioned above, the FE-SPH ACM is suitable for the penetration problem of aluminum and ceramic targets. Therefore, in this section we use FE-SPH ACM to investigate the anti-penetration problem of aluminum/ceramic composite targets with different combinations.

5.1. Computational Model

The model of a flat-headed projectile impacting a ceramic-aluminum alloy composite target plate was established using LS-DYNA. The projectile was modeled as a cylindrical body with a diameter of 6 mm and a length of 24 mm, and the material was aluminum alloy. The composite target plate was modeled as a square with dimensions of 100 mm \times 100 mm, and the thickness and material could be set according to different model. All elements in the model were hexahedral Lagrangian elements. When using the FE-SPH ACM for calculations, the target plate was set as a keyword (DEFINE_ADAPTIVE_SOLID_TO_SPH) to convert the FEM element into SPH element.

5.2. Simulation Analysis of Penetration of Composite Targets in Different Combinations

Firstly, FE-SPH ACM is used to numerically simulate and analyze composite target plates with different combinations. As shown in Figure 11, ceramic-aluminum alloy composite target plates with different combinations are set up. C/A represents ceramic material for the surface panel and aluminum alloy for the back panel, A/C represents aluminum alloy material for the surface panel and ceramic material for the back panel, and A/C/A represents a three-layer composite target plate with two layers of aluminum alloy sandwiching one layer of ceramic material. d_1 and d_2 represent the thickness of the composite target plate (red denotes the projectile, blue denotes the ceramic material, and green denotes the aluminum alloy material), and the different combinations are set as shown in Table 5. For composite target plates in different combinations, the total thickness of the composite target

plate is kept constant, fixed at 10 mm, and the proportion of the surface and back sections is changed. The table shows that there are three different proportions: 3/7, 5/5, and 7/3, which are used to explore the deformation characteristics and anti-penetration performance of ceramic and aluminum alloy composite target plates in different proportions.

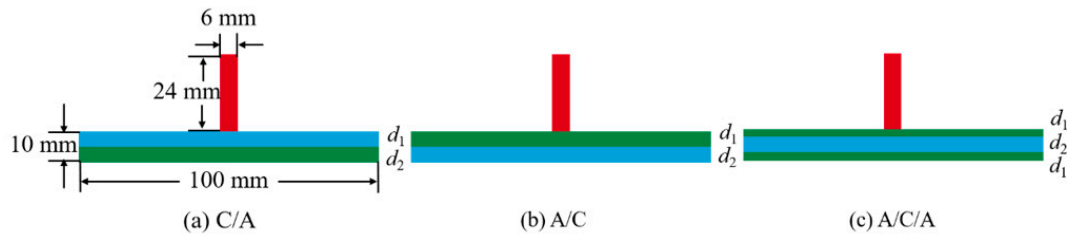


Figure 11. Composite target plates under different combinations. (a) C/A; (b) A/C; (c) A/C/A.

Table 5. The thickness settings of composite target plates under different combinations.

	No.	d_1 (mm)	d_2 (mm)
C/A	a	3	7
	b	5	5
	c	7	3
A/C	d	3	7
	e	5	5
	f	7	3
A/C/A	h	1.5	7
	i	2.5	5
	j	3.5	3

Then, the composite target material with a ceramic-to-aluminum alloy ratio of 5/5 is selected as the research object, and the propagation process of stress waves in different structural target plates is analyzed, as shown in Figure 12. Here, the velocity of the projectile is 1500 m/s. From the figure, it can be observed that stress waves propagate from the impact point to the surroundings. Due to differences in impedance, the size of stress waves in different materials can vary significantly, with stress values being higher in ceramic materials than in aluminum alloy materials. There is a sudden decrease in stress waves when they propagate from ceramic materials to aluminum alloy materials, and a sudden increase in stress waves when propagating from aluminum alloy materials to ceramic materials. At the boundary between materials, there is reflection of interface waves.

Figure 13 presents the images of each layer of composite target plates with a ceramic aluminum alloy ratio of 5/5 under different combinations at different times under the velocity of 1500 m/s. From the figure, it can be seen that when the combination is C/A, at 10 μ s, the ceramic elements of the first layer begin to fail and convert into SPH particles, resulting in the generation of cracks in the ceramic section, while the aluminum alloy changes are not significant. As time increases, at 30 μ s, the cracks in the ceramic continue to expand, and the elements of the aluminum alloy part begin to fail, creating pits and some of them converting into SPH particles. When the combination is A/C, the aluminum alloy part is first in contact with the projectile. At 10 μ s, the elements of the first layer of aluminum alloy fail and convert into SPH particles, creating pits, while some of the elements of the second layer of ceramics fail and convert into SPH particles, resulting in the formation of cracks. Subsequently, at 30 μ s, the aluminum alloy part is penetrated, and a large number of ceramic elements fail, leading to the formation of numerous cracks. The evolution process of the composite target plate in the A/C/A combination combines the characteristics of C/A and A/C. At 10 μ s, the elements of the first layer of aluminum alloy fail and convert into SPH particles, creating pits, while some of the elements of the second layer of ceramics fail and convert into SPH particles, leading to the formation of cracks,

while the changes in the third layer of aluminum alloy are not significant. Later, at 30 μs , the aluminum alloy of the first layer is penetrated, a large number of ceramic elements of the second layer fail and form a large number of cracks, and the elements of the third layer of aluminum alloy fail and convert into SPH particles, forming pits.

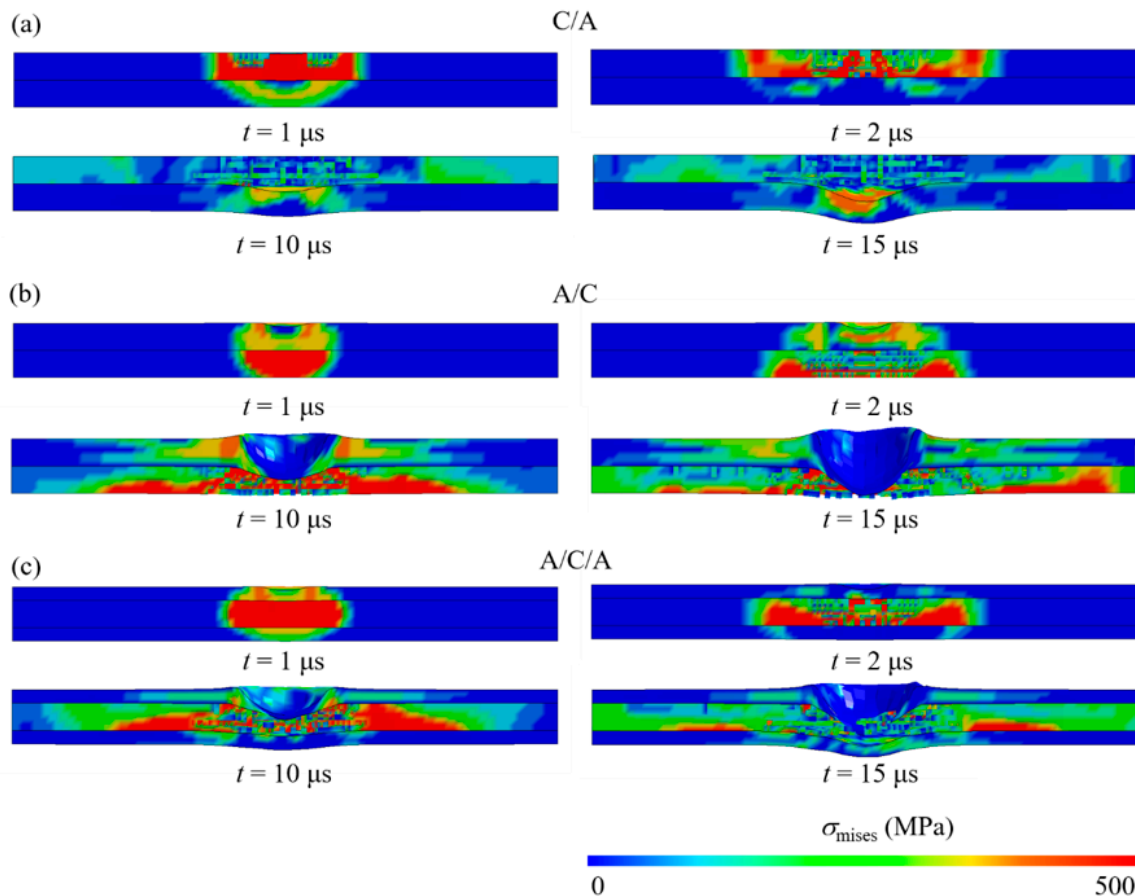


Figure 12. Von Mises stress evolution history of composite target plates with a ceramic aluminum alloy ratio of 5/5 under different combinations at different times under the velocity of 1500 m/s. (a) C/A; (b) A/C; (c) A/C/A.

Furthermore, we compare the residual velocity of the projectile penetrating the composite target plate with the variation of penetration velocity under different combinations, as shown in Figure 14. From Figure 14a, it can be seen that when the combination is C/A, the projectile cannot penetrate the composite target plate at lower velocities. The ballistic limit velocity of a composite target plate with a ceramic-to-aluminum alloy proportion of 3/7 is between 1200 and 1300 m/s, while that of a composite target plate with a ceramic-to-aluminum alloy proportion of 5/5 is between 1300 and 1400 m/s, and that of a composite target plate with a ceramic-to-aluminum alloy proportion of 7/3 is between 1400 and 1500 m/s. When the combination is A/C, as shown in Figure 14b, the projectile penetrates all the composite target plates, and the residual velocity of the projectile after penetration decreases with the increase in the ceramic proportion. When the combination is A/C/A, as shown in Figure 14c, the ballistic limit velocity of the composite target plate with a ceramic-to-aluminum alloy proportion of 3/7 is between 1200 and 1300 m/s, the ballistic limit velocity of the composite target plate with a ceramic-to-aluminum alloy proportion of 5/5 is between 1000 and 1100 m/s, and the ballistic limit velocity of the composite target plate with a ceramic-to-aluminum alloy proportion of 7/3 is between 1300 and 1400 m/s. In addition, we use the Lambert–Jonas approach [42] to describe the ballistic limit analyses.

This method is widely used in the analysis of the critical velocity of projectiles. The main equation is expressed as:

$$v_r = \alpha \left(v_p^n - v_{50}^n \right)^{1/n}$$

where v_p is the initial velocity of the projectile, v_r is the remaining velocity of the projectile, v_{50} is the ballistic limit velocity, and α and n are empirical parameters. Typically, $n = 2$, $\alpha = \sqrt{\frac{m}{m+M}}$, m represents the mass of the projectile, and M represents the mass ejected during the impact process. Based on the Lambert–Jonas approach, the calculation results show that the simulation results are in good agreement with the results obtained from the calculation formula. As the ceramic proportion increases, the remaining velocity of the projectile decreases, which reflects the enhancement of the anti-penetration performance of the composite target.

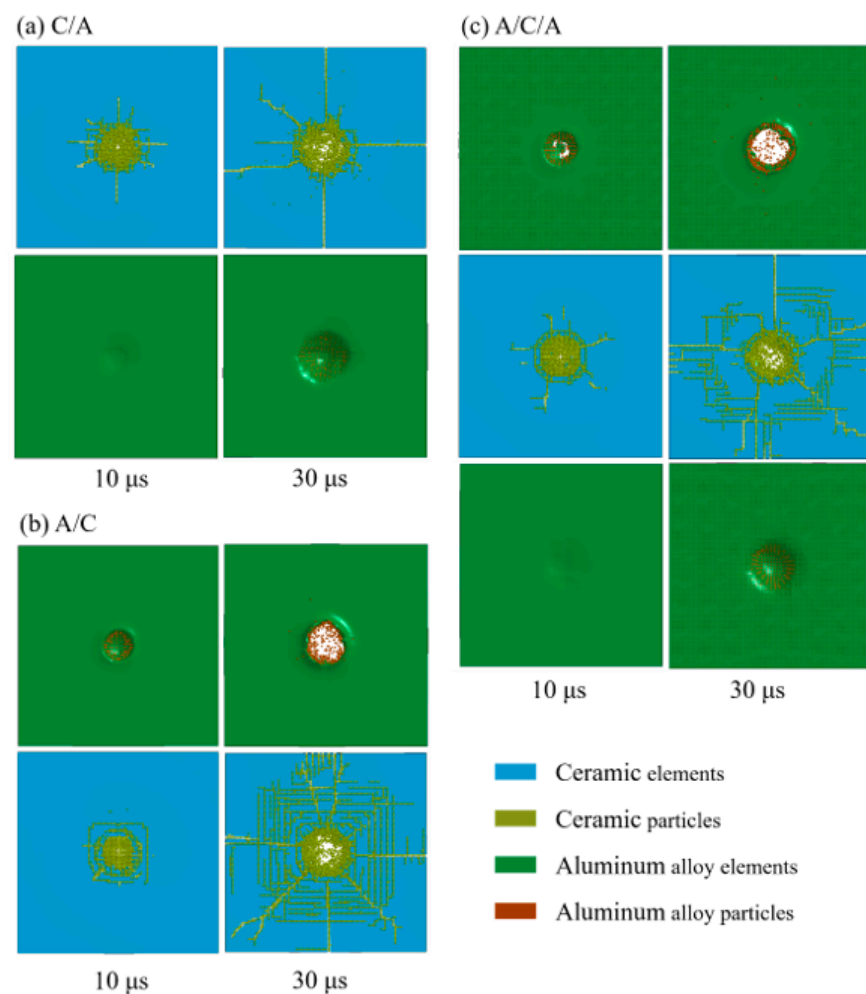


Figure 13. Images of each layer of composite target plates with a ceramic aluminum alloy ratio of 5/5 under different combinations at different times under the velocity of 1500 m/s. (a) C/A; (b) A/C; (c) A/C/A.

In summary, the composite target plate under C/A has the strongest resistance to penetration, followed by the composite target plate under the A/C/A. The composite target plate under the A/C has the weakest resistance to penetration. Additionally, the higher the ceramic proportion, the higher the ballistic limit velocity of the composite target plate. Obviously, increasing the ceramic proportion can enhance the anti-penetration performance of the composite target plate.

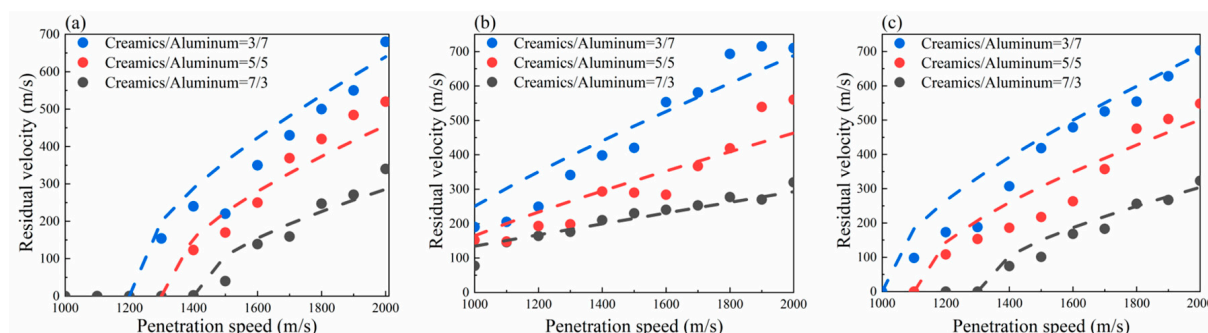


Figure 14. Curve of residual velocity of projectiles penetrating composite target plates under different combinations as a function of penetration velocity. (a) C/A; (b) A/C; (c) A/C/A.

6. Conclusions

In this work, numerical simulations of the projectile-target penetration problem were conducted using the FEM, SPH and the FE-SPH ACM using the LS-DYNA software package. By comparison with the experimental results, the accuracy of FE-SPH ACM was verified. Furthermore, the penetration resistance of aluminum/ceramic composite targets with different combinations was studied based on FE-SPH ACM. The main conclusions were as follows:

- (1) In the problem of a projectile penetrating an aluminum alloy target, the FE-SPH ACM had better accuracy in calculating the debris cloud head velocity and interface velocity, with an error of no more than 4% compared to the theoretical results. Moreover, FE-SPH ACM showed significantly greater precision in predicting the characteristic size of the fragment cloud compared to SPH, with an error rate reduced by almost half.
- (2) In the problem of a projectile penetrating ceramics, the FE-SPH ACM method was able to obtain complete images of ceramic debris clouds. Compared to the FEM and SPH, the residual velocity of the projectile simulated by FE-SPH ACM was highly consistent with the experimental results (with an error of 1.76%), thus verifying the rationality and accuracy of the FE-SPH method.
- (3) The anti-penetration performance of aluminum/ceramic composite targets in different combinations was studied based with FE-SPH ACM. The results showed that the composite target plate under the C/A had the strongest anti-penetration performance, followed by the composite target plate under the A/C/A. The composite target plate under the A/C had the weakest anti-penetration performance. Among them, for C/A, the ballistic limit velocities for ceramic-aluminum ratios of 3/7, 5/5, and 7/3 were approximately 1300 m/s, 1400 m/s, and 1500 m/s, respectively. Obviously, increasing the proportion of ceramic materials can enhance the anti-penetration performance of the composite target within the range of ceramic-aluminum ratio considered here.

Author Contributions: Conceptualization, J.S. and Y.S.; Investigation, T.H.; Validation, T.H., W.W. and J.S.; Methodology, T.H., W.W. and J.S.; Supervision, J.S.; Visualization, T.H.; Writing—original draft, T.H.; Writing—review and editing, W.W., J.S., Y.Z., Y.J., Y.M., Y.L. and Y.S. All authors have read and agreed to the published version of the manuscript.

Funding: This research received no external funding.

Data Availability Statement: The data used to support this research are available on request from the corresponding author.

Conflicts of Interest: The authors declare no conflict of interest.

References

1. Lu, W.J.; Li, B.; Li, J.H.; Hou, J.F.; Xu, X.W.; Zhang, L.M. Numerical simulation of dynamic response and failure of large-diameter thin-walled cylinder under vibratory penetration. *Ocean Eng.* **2022**, *249*, 110936. [[CrossRef](#)]
2. Liu, Y.; Huang, F.L.; Ma, A. Numerical simulations of oblique penetration into reinforced concrete targets. *Comput. Math. Appl.* **2011**, *61*, 2168–2171. [[CrossRef](#)]
3. Liu, Q.Q.; Wang, S.P.; Lin, X.; Cui, P.; Zhang, S. Numerical simulation on the anti-penetration performance of polyurea-core Weldox 460 E steel sandwich plates. *Compos. Struct.* **2020**, *236*, 111852. [[CrossRef](#)]
4. Lv, H.; He, Q.G.; Chen, X.W.; Han, P.F. Numerical simulation of impact crater formation and distribution of high-pressure polymorphs. *Acta Astronaut.* **2023**, *203*, 169–186. [[CrossRef](#)]
5. Cheng, Z.T.; Xiang, Z.; Song, Q. FEM-SPH adaptive method for analysis protection mechanism of BC ceramics. *Eng. Fail. Anal.* **2023**, *148*, 107207. [[CrossRef](#)]
6. Zhang, X.; Jia, G.H.; Huang, H. Numerical investigation of aluminum foam shield based on fractal theory and node-separation FEM. *Chin. J. Aeronaut.* **2011**, *24*, 734–740. [[CrossRef](#)]
7. Li, C.F.; Hu, N.; Yin, Y.J.; Sekine, H.; Fukunaga, H. Low-velocity impact-induced damage of continuous fiber-reinforced composite laminates. Part I. An FEM numerical model. *Compos. Part A Appl. Sci. Manuf.* **2002**, *33*, 1055–1062. [[CrossRef](#)]
8. Færgestad, R.M.; Holmen, J.K.; Berstad, T.; Cardone, T.; Ford, K.A.; Børvik, T. Coupled finite element-discrete element method (FEM/DEM) for modelling hypervelocity impacts. *Acta Astronaut.* **2023**, *203*, 296–307. [[CrossRef](#)]
9. Cui, X.; Liu, G.R.; Li, Z.R. A high-order edge-based smoothed finite element (ES-FEM) method with four-node triangular element for solid mechanics problems. *Eng. Anal. Bound. Elem.* **2023**, *151*, 490–502. [[CrossRef](#)]
10. Chakraborty, S.; Islam MR, I.; Shaw, A.; Ramachandra, L.S.; Reid, S.R. A computational framework for modelling impact induced damage in ceramic and ceramic-metal composite structures. *Compos. Struct.* **2017**, *164*, 263–276. [[CrossRef](#)]
11. Liu, Y.; Li, B.Z.; Wu, C.J.; Kong, L.F.; Zheng, Y.H. Smoothed particle hydrodynamics simulation and experimental analysis of SiC ceramic grinding mechanism. *Ceram. Int.* **2018**, *44*, 12194–12203. [[CrossRef](#)]
12. Silnikov, M.; Guk, I.; Mikhaylin, A.; Nechunaev, A. Efficiency of needle structure at hypervelocity impact. *Acta Astronaut.* **2018**, *50*, 73–80. [[CrossRef](#)]
13. Horabik, J.; Sochan, A.; Beczek, M.; Mazur, R.; Ryzak, M.; Parafiniuk, P.; Kobylka, R.; Bieganowski, A. Discrete element method simulations and experimental study of interactions in 3D granular bedding during low-velocity impact. *Powder Technol.* **2018**, *340*, 52–67. [[CrossRef](#)]
14. Wang, Q.; Zhang, Q.; Huang, F.; Long, R.; Gong, Z. An analytical model for the motion of debris clouds induced by hypervelocity impact projectiles with different shapes on multi-plate structures. *Int. J. Impact Eng.* **2014**, *74*, 157–164. [[CrossRef](#)]
15. Ju, A.J.; Zhang, R.; Cai, Y.T. Study on characteristics and prediction model of jet impact concrete crushing based on SPH modeling. *Structures* **2022**, *44*, 1523–1531. [[CrossRef](#)]
16. Johnson, G.R. Linking of Lagrangian particle methods to standard finite element methods for high velocity impact simulation. *Nucl. Eng. Des.* **1994**, *150*, 265–274. [[CrossRef](#)]
17. Fernández, M.S.; Bonet, J.; Huerta, A. Continuous blending of SPH with finite elements. *Comput. Struct.* **2004**, *83*, 1448–1458. [[CrossRef](#)]
18. Rabczuk, T.; Xiao, S.P.; Sauer, M. Coupling of mesh-free method with finite elements: Basic concepts and test results. *Commun. Numer. Methods Eng.* **2006**, *22*, 1031–1065. [[CrossRef](#)]
19. Johnson, G.R.; Stryk, R.A.; Beissel, S.R.; Holmquist, T.J. An algorithm to automatically convert distorted finite elements into meshless particles during dynamic deformation. *Int. J. Impact Eng.* **2002**, *27*, 997–1013. [[CrossRef](#)]
20. He, Q.G.; Chen, X.W.; Chen, J.F. Finite element-smoothed particle hydrodynamics adaptive method in simulating debris cloud. *Acta Astronaut.* **2020**, *175*, 99–117. [[CrossRef](#)]
21. He, Q.G.; Chen, J.F.; Chen, X.W. Velocity-space analysis method for hazardous fragments in debris clouds. *Int. J. Impact Eng.* **2020**, *161*, 104087. [[CrossRef](#)]
22. Wen, K.; Chen, X.W.; Chi, R.Q.; Lu, Y.G. Analysis on the fragmentation pattern of sphere hypervelocity impacting on thin plate. *Int. J. Impact Eng.* **2020**, *146*, 103721.1–103721.15. [[CrossRef](#)]
23. Scazzosi, R.; Giglio, M.; Manes, A. FE coupled to SPH numerical model for the simulation of high-velocity impact on ceramic based ballistic shields. *Ceram. Int.* **2020**, *46*, 23760–23772. [[CrossRef](#)]
24. Kala, J.; Hušek, M. Improved element erosion function for concrete-like materials with the SPH method. *Shock Vib.* **2016**, *2016*, 4593749. [[CrossRef](#)]
25. Cottrell, M.G.; Yu, J.; Owen, D.R.J. The adaptive and erosive numerical modelling of confined boron carbide subjected to large-scale dynamic loadings with element conversion to undeformable meshless particles. *Int. J. Impact Eng.* **2003**, *28*, 1017–1035. [[CrossRef](#)]
26. Johnson, G.R.; Stryk, R.A. Conversion of 3D distorted elements into meshless particles during dynamic deformation. *Int. J. Impact Eng.* **2003**, *28*, 947–966. [[CrossRef](#)]
27. Bless, S. Bumper debris cloud structure estimated by shock calculations. *J. Phys. IV* **1991**, *1*, 903–908. [[CrossRef](#)]
28. Børvik, T.; Langseth, M.; Hopperstad, O.S.; Malo, K.A. Perforation of 12 mm thick steel plates by 20 mm diameter projectiles with flat, hemispherical and conical noses: Part I: Experimental study. *Int. J. Impact Eng.* **2002**, *27*, 19–35. [[CrossRef](#)]

29. Kpenyigba, K.M.; Jankowiak, T.; Rusinek, A.; Pesci, R.; Wang, B. Effect of projectile nose shape on ballistic resistance of interstitial-free steel sheets. *Int. J. Impact Eng.* **2015**, *79*, 83–94. [[CrossRef](#)]
30. Xing, B.; Zhang, D.; Guo, Z.; Hou, Y.; Guo, R.; Liu, R.; Chen, L.; Zhou, H.; Yang, Y.; Luo, J. Analysis of the mass of behind-armor debris generated by RHA subjected to normal penetration of variable cross-section EFP. *Def. Technol.* **2019**, *15*, 390–397. [[CrossRef](#)]
31. Liu, J.; Liu, C.; Zhang, X.; Li, P.; Wei, H.; Xiong, W.; Tan, M. Research on the penetration characteristics of elliptical cross-section projectile into semi-infinite metal targets. *Int. J. Impact Eng.* **2023**, *173*, 104438. [[CrossRef](#)]
32. Wei, H.; Zhang, X.; Liu, C.; Xiong, W.; Chen, H.; Tan, M. Oblique penetration of ogive-nosed projectile into aluminum alloy targets. *Int. J. Impact Eng.* **2021**, *148*, 1032745. [[CrossRef](#)]
33. Deng, Y.F.; Jia, H.R.; Li, J.F. Numerical investigation of 2A12 aluminum alloy thin targets impacted under oblique angles by blunt-nosed high-strength projectiles. *Mater. Today Commun.* **2022**, *30*, 103118. [[CrossRef](#)]
34. Piekutowski, A.J. Characteristics of debris clouds produced by hypervelocity impact of aluminum spheres with thin aluminum plates. *Int. J. Impact Eng.* **1993**, *14*, 573–586. [[CrossRef](#)]
35. Johnson, G.R.; Cook, W. Fracture characteristics of three metals subjected to various strains, strain rates, temperatures and pressures. *Eng. Fract. Mech.* **1985**, *21*, 31–48. [[CrossRef](#)]
36. Roeder, B.A.; Sun, C.T. Dynamic penetration of alumina/aluminum laminates: Experiments and modeling. *Int. J. Impact Eng.* **2001**, *25*, 169–185. [[CrossRef](#)]
37. Nemat-Nasser, S.; Sarva, S.; Isaacs, J.B.; Lischer, D.W. Novel ideas in multifunctional ceramic design. *Ceram. Trans.* **2002**, *134*, 511–525.
38. Li, J.C.; Chen, X.W.; Huang, F.L. FEM analysis on the self-sharpening behavior of tungsten fiber/metallic glass matrix composite long rod. *Int. J. Impact Eng.* **2015**, *86*, 67–83. [[CrossRef](#)]
39. Tian, S.Y.; Song, S.C. Dynamic properties test of steel 603 and 675 and establishment of constitutive relations. *J. Ningbo Univ.* **2003**, *16*, 462–465.
40. Holmquist, T.; Johnson, G. Response of silicon carbide to high velocity impact. *J. Appl. Phys.* **2002**, *91*, 5858–5866. [[CrossRef](#)]
41. Johnson, G.; Holmquist, T. An improved computational constitutive model for brittle materials. In *AIP Conference Proceedings*; American Institute of Physics: New York, NY, USA, 1994; pp. 981–984.
42. Lambert, J.P.; Jonas, G.H. *Towards Standardization of In-Terminal Ballistic Testing Velocity Representation*; Report BRL-R-1852; Ballistic Res. Lab.: Aberdeen, MD, USA, 1976.

Disclaimer/Publisher’s Note: The statements, opinions and data contained in all publications are solely those of the individual author(s) and contributor(s) and not of MDPI and/or the editor(s). MDPI and/or the editor(s) disclaim responsibility for any injury to people or property resulting from any ideas, methods, instructions or products referred to in the content.